



Measurement of the differential cross sections for isolated direct photon pair production in $p\bar{p}$ collisions at $\sqrt{s} = 1.96$ TeV



D0 Collaboration

V.M. Abazov^{ag}, B. Abbott^{bq}, B.S. Acharya^{aa}, M. Adams^{av}, T. Adams^{at}, G.D. Alexeev^{ag}, G. Alkhazov^{ak}, A. Alton^{bf,1}, V.B. Anikeev^{aj}, A. Askew^{at}, S. Atkins^{bd}, K. Augsten^g, C. Avila^e, F. Badaud^j, L. Bagby^{au}, B. Baldin^{au}, D.V. Bandurin^{at}, S. Banerjee^{aa}, E. Barberis^{be}, P. Baringer^{bc}, J.F. Bartlett^{au}, U. Bassler^o, V. Bazterra^{av}, A. Bean^{bc}, M. Begalli^b, L. Bellantoni^{au}, S.B. Beri^y, G. Bernardiⁿ, R. Bernhard^t, I. Bertram^{ao}, M. Besançon^o, R. Beuselinck^{ap}, P.C. Bhat^{au}, S. Bhatia^{bh}, V. Bhatnagar^y, G. Blazey^{aw}, S. Blessing^{at}, K. Bloom^{bi}, A. Boehnlein^{au}, D. Boline^{bn}, E.E. Boos^{ai}, G. Borissov^{ao}, A. Brandt^{bt}, O. Brandt^u, R. Brock^{bg}, A. Bross^{au}, D. Brownⁿ, X.B. Bu^{au}, M. Buehler^{au}, V. Buescher^v, V. Bunichev^{ai}, S. Burdin^{ao,2}, C.P. Buszello^{am}, E. Camacho-Pérez^{ad}, B.C.K. Casey^{au}, H. Castilla-Valdez^{ad}, S. Caughron^{bg}, S. Chakrabarti^{bn}, D. Chakraborty^{aw}, K.M. Chan^{ba}, A. Chandra^{bv}, E. Chapon^o, G. Chen^{bc}, S.W. Cho^{ac}, S. Choi^{ac}, B. Choudhary^z, S. Cihangir^{au}, D. Claes^{bi}, J. Clutter^{bc}, M. Cooke^{au}, W.E. Cooper^{au}, M. Corcoran^{bv}, F. Couderc^o, M.-C. Cousinou^l, D. Cutts^{bs}, A. Das^{ar}, G. Davies^{ap}, S.J. de Jong^{ae,af}, E. De La Cruz-Burelo^{ad}, F. Déliot^o, R. Demina^{bm}, D. Denisov^{au}, S.P. Denisov^{aj}, S. Desai^{au}, C. Deterre^{u,4}, K. DeVaughan^{bi}, H.T. Diehl^{au}, M. Diesburg^{au}, P.F. Ding^{aq}, A. Dominguez^{bi}, A. Dubey^z, L.V. Dudko^{ai}, A. Duperrin^l, S. Dutt^y, A. Dyshkant^{aw}, M. Eads^{aw}, D. Edmunds^{bg}, J. Ellison^{as}, V.D. Elvira^{au}, Y. Enariⁿ, H. Evans^{ay}, V.N. Evdokimov^{aj}, L. Feng^{aw}, T. Ferbel^{bm}, F. Fiedler^v, F. Filthaut^{ae,af}, W. Fisher^{bg}, H.E. Fisk^{au}, M. Fortner^{aw}, H. Fox^{ao}, S. Fuess^{au}, A. Garcia-Bellido^{bm}, J.A. García-González^{ad}, G.A. García-Guerra^{ad,3}, V. Gavrilov^{ah}, W. Geng^{l,bg}, C.E. Gerber^{av}, Y. Gershtein^{bj}, G. Ginther^{au,bm}, G. Golovanov^{ag}, P.D. Grannis^{bn}, S. Greder^p, H. Greenlee^{au}, G. Grenier^{q,r}, Ph. Gris^j, J.-F. Grivaz^m, A. Grohsjean^{o,4}, S. Grünendahl^{au}, M.W. Grünewald^{ab}, T. Guillemin^m, G. Gutierrez^{au}, P. Gutierrez^{bq}, J. Haley^{be}, L. Han^d, K. Harder^{aq}, A. Harel^{bm}, J.M. Hauptman^{bb}, J. Hays^{ap}, T. Head^{aq}, T. Hebbeker^s, D. Hedin^{aw}, H. Hegab^{br}, A.P. Heinson^{as}, U. Heintz^{bs}, C. Hensel^u, I. Heredia-De La Cruz^{ad}, K. Herner^{bf}, G. Hesketh^{aq,6}, M.D. Hildreth^{ba}, R. Hirosky^{bw}, T. Hoang^{at}, J.D. Hobbs^{bn}, B. Hoeneisenⁱ, J. Hogan^{bv}, M. Hohlfeld^v, I. Howley^{bt}, Z. Hubacek^{g,o}, V. Hynek^g, I. Iashvili^{bl}, Y. Ilchenko^{bu}, R. Illingworth^{au}, A.S. Ito^{au}, S. Jabeen^{bs}, M. Jaffré^m, A. Jayasinghe^{bq}, M.S. Jeong^{ac}, R. Jesik^{ap}, P. Jiang^d, K. Johns^{ar}, E. Johnson^{bg}, M. Johnson^{au}, A. Jonckheere^{au}, P. Jonsson^{ap}, J. Joshi^{as}, A.W. Jung^{au}, A. Juste^{al}, E. Kajfasz^l, D. Karmanov^{ai}, I. Katsanos^{bi}, R. Kehoe^{bu}, S. Kermiche^l, N. Khalatyan^{au}, A. Khanov^{br}, A. Kharchilava^{bl}, Y.N. Kharzhev^{ag}, I. Kiselevich^{ah}, J.M. Kohli^y, A.V. Kozelov^{aj}, J. Kraus^{bh}, A. Kumar^{bl}, A. Kupco^h, T. Kurča^{q,r}, V.A. Kuzmin^{ai}, S. Lammers^{ay}, P. Lebrun^{q,r}, H.S. Lee^{ac}, S.W. Lee^{bb}, W.M. Lee^{at}, X. Lei^{ar}, J. Lellouchⁿ, D. Liⁿ, H. Li^{bw}, L. Li^{as}, Q.Z. Li^{au}, J.K. Lim^{ac}, D. Lincoln^{au}, J. Linnemann^{bg}, V.V. Lipaev^{aj}, R. Lipton^{au}, H. Liu^{bu}, Y. Liu^d, A. Lobodenko^{ak}, M. Lokajicek^h, R. Lopes de Sa^{bn}, R. Luna-Garcia^{ad,7}, A.L. Lyon^{au}, A.K.A. Maciel^a, R. Magaña-Villalba^{ad}, S. Malik^{bi}, V.L. Malyshev^{ag}, J. Mansour^u, J. Martínez-Ortega^{ad}, R. McCarthy^{bn}, C.L. McGivern^{aq},

M.M. Meijer^{ae,af}, A. Melnitchouk^{au}, D. Menezes^{aw}, P.G. Mercadante^c, M. Merkin^{ai},
 A. Meyer^s, J. Meyer^{u,10}, F. Miconi^p, N.K. Mondal^{aa}, M. Mulhearn^{bw}, E. Nagy^l,
 M. Naimuddin^z, M. Narain^{bs}, R. Nayyar^{ar}, H.A. Neal^{bf}, J.P. Negret^e, P. Neustroev^{ak},
 H.T. Nguyen^{bw}, T. Nunnemann^w, J. Orduna^{bv}, N. Osman^l, J. Osta^{ba}, M. Padilla^{as}, A. Pal^{bt},
 N. Parashar^{az}, V. Parihar^{bs}, S.K. Park^{ac}, R. Partridge^{bs,5}, N. Parua^{ay}, A. Patwa^{bo,11},
 B. Penning^{au}, M. Perfilov^{ai}, Y. Peters^u, K. Petridis^{aq}, G. Petrillo^{bm}, P. Pétroff^m,
 M.-A. Pleier^{bo}, P.L.M. Podesta-Lerma^{ad,8}, V.M. Podstavkov^{au}, A.V. Popov^{aj}, M. Prewitt^{bv},
 D. Price^{ay}, N. Prokopenko^{aj}, J. Qian^{bf}, A. Quadt^u, B. Quinn^{bh}, M.S. Rangel^a, P.N. Ratoff^{ao},
 I. Razumov^{aj}, I. Ripp-Baudot^p, F. Rizatdinova^{br}, M. Rominsky^{au}, A. Ross^{ao}, C. Royon^o,
 P. Rubinov^{au}, R. Ruchti^{ba}, G. Sajot^k, P. Salcido^{aw}, A. Sánchez-Hernández^{ad}, M.P. Sanders^w,
 A.S. Santos^{a,9}, G. Savage^{au}, L. Sawyer^{bd}, T. Scanlon^{ap}, R.D. Schamberger^{bn}, Y. Scheglov^{ak},
 H. Schellman^{ax}, C. Schwanenberger^{aq}, R. Schwienhorst^{bg}, J. Sekaric^{bc}, H. Severini^{bq},
 E. Shabalina^u, V. Shary^o, S. Shaw^{bg}, A.A. Shchukin^{aj}, R.K. Shivpuri^z, V. Simak^g,
 P. Skubic^{bq}, P. Slattery^{bm}, D. Smirnov^{ba}, K.J. Smith^{bl}, G.R. Snow^{bi}, J. Snow^{bp}, S. Snyder^{bo},
 S. Söldner-Rembold^{aq}, L. Sonnenschein^s, K. Soustruznik^f, J. Stark^k, D.A. Stoyanova^{aj},
 M. Strauss^{bq}, L. Suter^{aq}, P. Svoisky^{bq}, M. Titov^o, V.V. Tokmenin^{ag}, V. Trusov^{an},
 Y.-T. Tsai^{bm}, D. Tsybychev^{bn}, B. Tuchming^o, C. Tully^{bk}, L. Uvarov^{ak}, S. Uvarov^{ak},
 S. Uzunyan^{aw}, R. Van Kooten^{ay}, W.M. van Leeuwen^{ae}, N. Varelas^{av}, E.W. Varnes^{ar},
 I.A. Vasilyev^{aj}, A.Y. Verkheev^{ag}, L.S. Vertogradov^{ag}, M. Verzocchi^{au}, M. Vesterinen^{aq},
 D. Vilanova^o, P. Vokac^g, H.D. Wahl^{at}, M.H.L.S. Wang^{au}, J. Warchol^{ba}, G. Watts^{bx},
 M. Wayne^{ba}, J. Weichert^v, L. Welty-Rieger^{ax}, A. White^{bt}, D. Wicke^x, M.R.J. Williams^{ao},
 G.W. Wilson^{bc}, M. Wobisch^{bd}, D.R. Wood^{be}, T.R. Wyatt^{aq}, Y. Xie^{au}, R. Yamada^{au},
 S. Yang^d, T. Yasuda^{au}, Y.A. Yatsunenko^{ag}, W. Ye^{bn}, Z. Ye^{au}, H. Yin^{au}, K. Yip^{bo},
 S.W. Youn^{au}, J.M. Yu^{bf}, J. Zennamo^{bl}, T.G. Zhao^{aq}, B. Zhou^{bf}, J. Zhu^{bf}, M. Zielinski^{bm},
 D. Zieminska^{ay}, L. Zivkovicⁿ

^a LAFEX, Centro Brasileiro de Pesquisas Físicas, Rio de Janeiro, Brazil^b Universidade do Estado do Rio de Janeiro, Rio de Janeiro, Brazil^c Universidade Federal do ABC, Santo André, Brazil^d University of Science and Technology of China, Hefei, People's Republic of China^e Universidad de los Andes, Bogotá, Colombia^f Charles University, Faculty of Mathematics and Physics, Center for Particle Physics, Prague, Czech Republic^g Czech Technical University in Prague, Prague, Czech Republic^h Center for Particle Physics, Institute of Physics, Academy of Sciences of the Czech Republic, Prague, Czech Republicⁱ Universidad San Francisco de Quito, Quito, Ecuador^j LPC, Université Blaise Pascal, CNRS/IN2P3, Clermont, France^k LPSC, Université Joseph Fourier Grenoble 1, CNRS/IN2P3, Institut National Polytechnique de Grenoble, Grenoble, France^l CPPM, Aix-Marseille Université, CNRS/IN2P3, Marseille, France^m LAL, Université Paris-Sud, CNRS/IN2P3, Orsay, Franceⁿ LPNHE, Universités Paris VI and VII, CNRS/IN2P3, Paris, France^o CEA, Irfu, SPP, Saclay, France^p IPHC, Université de Strasbourg, CNRS/IN2P3, Strasbourg, France^q IPNL, Université Lyon 1, CNRS/IN2P3, Villeurbanne, France^r Université de Lyon, Lyon, France^s III. Physikalisches Institut A, RWTH Aachen University, Aachen, Germany^t Physikalisches Institut, Universität Freiburg, Freiburg, Germany^u II. Physikalisches Institut, Georg-August-Universität Göttingen, Göttingen, Germany^v Institut für Physik, Universität Mainz, Mainz, Germany^w Ludwig-Maximilians-Universität München, München, Germany^x Fachbereich Physik, Bergische Universität Wuppertal, Wuppertal, Germany^y Panjab University, Chandigarh, India^z Delhi University, Delhi, India^{aa} Tata Institute of Fundamental Research, Mumbai, India^{ab} University College Dublin, Dublin, Ireland^{ac} Korea Detector Laboratory, Korea University, Seoul, Republic of Korea^{ad} CINVESTAV, Mexico City, Mexico^{ae} Nikhef, Science Park, Amsterdam, The Netherlands^{af} Radboud University Nijmegen, Nijmegen, The Netherlands^{ag} Joint Institute for Nuclear Research, Dubna, Russia^{ah} Institute for Theoretical and Experimental Physics, Moscow, Russia^{ai} Moscow State University, Moscow, Russia^{aj} Institute for High Energy Physics, Protvino, Russia^{ak} Petersburg Nuclear Physics Institute, St. Petersburg, Russia^{al} Institució Catalana de Recerca i Estudis Avançats (ICREA) and Institut de Física d'Altes Energies (IFAE), Barcelona, Spain^{am} Uppsala University, Uppsala, Sweden^{an} Taras Shevchenko National University of Kyiv, Kiev, Ukraine

- ^{a0} Lancaster University, Lancaster LA1 4YB, United Kingdom
^{aP} Imperial College London, London SW7 2AZ, United Kingdom
^{aQ} The University of Manchester, Manchester M13 9PL, United Kingdom
^{aR} University of Arizona, Tucson, AZ 85721, USA
^{aS} University of California Riverside, Riverside, CA 92521, USA
^{aT} Florida State University, Tallahassee, FL 32306, USA
^{aU} Fermi National Accelerator Laboratory, Batavia, IL 60510, USA
^{aV} University of Illinois at Chicago, Chicago, IL 60607, USA
^{aW} Northern Illinois University, DeKalb, IL 60115, USA
^{aX} Northwestern University, Evanston, IL 60208, USA
^{aY} Indiana University, Bloomington, IN 47405, USA
^{aZ} Purdue University Calumet, Hammond, IN 46323, USA
^{ba} University of Notre Dame, Notre Dame, IN 46556, USA
^{bb} Iowa State University, Ames, IA 50011, USA
^{bc} University of Kansas, Lawrence, KS 66045, USA
^{bd} Louisiana Tech University, Ruston, LA 71272, USA
^{be} Northeastern University, Boston, MA 02115, USA
^{bf} University of Michigan, Ann Arbor, MI 48109, USA
^{bg} Michigan State University, East Lansing, MI 48824, USA
^{bh} University of Mississippi, University, MS 38677, USA
^{bi} University of Nebraska, Lincoln, NE 68588, USA
^{bj} Rutgers University, Piscataway, NJ 08855, USA
^{bk} Princeton University, Princeton, NJ 08544, USA
^{bl} State University of New York, Buffalo, NY 14260, USA
^{bm} University of Rochester, Rochester, NY 14627, USA
^{bn} State University of New York, Stony Brook, NY 11794, USA
^{bo} Brookhaven National Laboratory, Upton, NY 11973, USA
^{bP} Langston University, Langston, OK 73050, USA
^{bQ} University of Oklahoma, Norman, OK 73019, USA
^{bR} Oklahoma State University, Stillwater, OK 74078, USA
^{bS} Brown University, Providence, RI 02912, USA
^{bT} University of Texas, Arlington, TX 76019, USA
^{bU} Southern Methodist University, Dallas, TX 75275, USA
^{bV} Rice University, Houston, TX 77005, USA
^{bW} University of Virginia, Charlottesville, VA 22904, USA
^{bX} University of Washington, Seattle, WA 98195, USA

ARTICLE INFO

Article history:

Received 19 January 2013

Received in revised form 18 June 2013

Accepted 18 June 2013

Available online 2 July 2013

Editor: M. Doser

ABSTRACT

We present measurements of direct photon pair production cross sections using 8.5 fb^{-1} of data collected with the D0 detector at the Fermilab Tevatron $p\bar{p}$ collider. The results are presented as differential distributions of the photon pair invariant mass $d\sigma/dM_{\gamma\gamma}$, pair transverse momentum $d\sigma/dp_T^{\gamma\gamma}$, azimuthal angle between the photons $d\sigma/d\Delta\phi_{\gamma\gamma}$, and polar scattering angle in the Collins-Soper frame $d\sigma/d|\cos\theta^*|$. Measurements are performed for isolated photons with transverse momenta $p_T^\gamma > 18$ (17) GeV for the leading (next-to-leading) photon in p_T , pseudorapidities $|\eta^\gamma| < 0.9$, and a separation in η - ϕ space $\Delta\mathcal{R}_{\gamma\gamma} > 0.4$. We present comparisons with the predictions from Monte Carlo event generators DIPHOX and RESBOS implementing QCD calculations at next-to-leading order, $2\gamma\text{NNLO}$ at next-to-next-to-leading order, and SHERPA using matrix elements with higher-order real emissions matched to parton shower.

© 2013 Elsevier B.V. All rights reserved.

Precise knowledge of the direct diphoton (DDP) production differential cross section is a cornerstone of the search for the standard model (SM) Higgs boson by experiments at the Large Hadron Collider [1,2] and the Tevatron [3–5]. The term “direct” means that these photons do not result from mesons, for example, π^0 , η , ω ,

or K_S^0 decays. DDP production is also a significant background in searches for Kaluza–Klein [6] or Randall–Sundrum [7] gravitons decaying into two photons, as well as other new phenomena processes, such as decays of heavy resonances [8] or cascade decays of supersymmetric particles [9]. For these searches, DDP production is an irreducible background, and it is crucial to have a detailed understanding of the distributions of key kinematic variables [10].

In addition to investigating physics beyond the SM, DDP production processes are important for studying quantum chromodynamics (QCD) and measuring parton distribution functions (PDFs). DDP production cross sections have been examined at fixed-target [11,12] and collider experiments [13–18]. DDP events at the Tevatron $p\bar{p}$ collider are produced predominantly through quark–antiquark annihilation $q\bar{q} \rightarrow \gamma\gamma$ and gluon–gluon fusion ($gg \rightarrow \gamma\gamma$) via a quark-loop diagram. The matrix element (ME) for the latter process is suppressed by α_s^2 relative to $q\bar{q}$ annihilation, but its total production rate at low $\gamma\gamma$ invariant mass ($M_{\gamma\gamma}$) and intermediate $\gamma\gamma$ transverse momentum ($p_T^{\gamma\gamma}$) is quite significant due to the relatively large values of the gluon PDFs

¹ Visitor from Augustana College, Sioux Falls, SD, USA.² Visitor from The University of Liverpool, Liverpool, UK.³ Visitor from UPIITA-IPN, Mexico City, Mexico.⁴ Visitor from DESY, Hamburg, Germany.⁵ Visitor from SLAC, Menlo Park, CA, USA.⁶ Visitor from University College London, London, UK.⁷ Visitor from Centro de Investigacion en Computacion – IPN, Mexico City, Mexico.⁸ Visitor from ECFM, Universidad Autonoma de Sinaloa, Culiacán, Mexico.⁹ Visitor from Universidade Estadual Paulista, São Paulo, Brazil.¹⁰ Visitor from Karlsruhe Institut für Technologie (KIT) – Steinbuch Centre for Computing (SCC).¹¹ Visitor from Office of Science, U.S. Department of Energy, Washington, DC 20585, USA.

in that kinematic region. By the same argument, gluon–gluon fusion becomes even more important at the LHC [19]. DDP events may also originate from processes such as $qg \rightarrow q\gamma$, $q\bar{q} \rightarrow g\gamma$, and $gg \rightarrow q\bar{q}$, where a photon with large transverse momentum is radiated from the final state parton. These processes, being nearly collinear, require the introduction of a fragmentation function in perturbative QCD (pQCD) calculations [19]. Photon isolation requirements reduce the contribution of such fragmentation events. However, their contribution may be still quite large at low $\gamma\gamma$ azimuthal angle difference ($\Delta\phi_{\gamma\gamma}$) and for intermediate $p_T^{\gamma\gamma}$ [19,20], which is the DDP transverse momentum.

In this Letter, we present measurements of differential cross sections of DDP production using the dataset collected at the Fermilab Tevatron D0 experiment between June 2006 and September 2011. The dataset corresponds to an integrated luminosity of $8.5 \pm 0.5 \text{ fb}^{-1}$ [37].

Measurements are performed as functions of $M_{\gamma\gamma}$, $p_T^{\gamma\gamma}$, $\Delta\phi_{\gamma\gamma}$, and $|\cos\theta^*|$, the absolute value of the cosine of the polar scattering angle of the diphoton system in the Collins–Soper frame [21]. Here we approximate $|\cos\theta^*|$ by $|\tanh[(\eta_1 - \eta_2)/2]|$, where $\eta_{1,2}$ are the pseudorapidities [22] of the leading and next-to-leading photons ranked by p_T . These four variables emphasize different phenomena in the diphoton production mechanism. $M_{\gamma\gamma}$ usually serves as a probe for new phenomena searches [1,2,6–8] and PDFs. The $p_T^{\gamma\gamma}$ and $\Delta\phi_{\gamma\gamma}$ shapes are mostly sensitive to the initial state gluon radiation and fragmentation effects. The $|\cos\theta^*|$ angle is sensitive to PDFs and spin correlations in the final state. In contrast with the previous D0 measurement [15], in this analysis we do not impose explicit minimum requirements on $M_{\gamma\gamma}$ or $\Delta\phi_{\gamma\gamma}$, nor do we require that $M_{\gamma\gamma} > p_T^{\gamma\gamma}$, making the measurements more universal. By separating the data into two subsets, with $\Delta\phi_{\gamma\gamma} \geq \pi/2$ and $\Delta\phi_{\gamma\gamma} < \pi/2$, we isolate regions with smaller and larger expected relative contributions from the fragmentation processes.

We compare our results with the theoretical predictions generated using the DIPHOX [19], RESBOS [10,23,24], $2\gamma_{\text{NNLO}}$ [25] and SHERPA [26] event generators. The general multipurpose generator approach is to employ interleaved QCD and quantum electrodynamics (QED) parton shower (PS) to describe initial and final state radiation. The SHERPA Monte Carlo (MC) event generator improves this technique by including higher-order real-emission matrix elements [27]. Matching between partons coming from real emissions in the ME and jets from PS is done at some (hardness) scale Q_{cut} defined following the prescriptions given in Ref. [27]. We use events generated with all MEs with two photons and up to two hard partons. However, the ME for gluon–gluon scattering $gg \rightarrow \gamma\gamma$ in SHERPA does not have real parton emissions. As shown in Ref. [27], SHERPA provides a good description of the fragmentation function measured at LEP at high fractions of the jet energy carried by the photon, corresponding to tight photon isolation cuts. The loop corrections matching the higher order MEs are missing in SHERPA, which can make predictions significantly scale-dependent and may lead to underestimation of $\gamma\gamma$ rates. In the SHERPA version used in this paper [26], the inherent next-to-leading-logarithmic effect of correlated emissions is invoked in parton-shower simulations by appropriately choosing a scale factor for the argument of the running strong coupling constant [28–30]. The DIPHOX and RESBOS packages provide predictions at next-to-leading order (NLO) in pQCD, with the $gg \rightarrow \gamma\gamma$ process considered only at the leading order approximation in DIPHOX. Also, in DIPHOX, explicit single and double parton-to-photon fragmentation processes are included at NLO accuracy, while in RESBOS, rates of fragmentation processes are approximated by a function. Only in RESBOS there are the effects of soft and collinear initial state gluon emissions resummed to all orders [24]. The resummation should be important for a correct description of the $p_T^{\gamma\gamma}$ distribution close

to zero and the $\Delta\phi_{\gamma\gamma}$ distribution close to π . The $2\gamma_{\text{NNLO}}$ generator, which appeared recently, exploits the $p_T^{\gamma\gamma}$ subtraction formalism [31] that handles the unphysical infra-red divergences up to next-to-next-to-leading order (NNLO). It takes into account most diagrams ($q\bar{q}$ and qg scatterings) at $\mathcal{O}(\alpha_s^2)$ accuracy; however, in the current calculations, there is a partial higher-order correction to the $gg \rightarrow \gamma\gamma$ box diagram and no soft gluon resummation is applied. Additionally, it does not take into account the fragmentation contributions.

The D0 detector, where the DDP measurements are performed, is a general purpose detector described in detail elsewhere [32, 34,35]. The sub-detectors used in this analysis to trigger events and reconstruct photons are the calorimeter, the central tracking system, and the central preshower. The muon detection system is used to compare data and MC simulation sets of $Z \rightarrow \mu^+\mu^- + \gamma$ events to obtain data-to-MC scale factors for reconstruction efficiency. The central tracking system, used to reconstruct tracks of charged particles, consists of a silicon micro-strip detector (SMT) and a central fiber track detector (CFT), both embedded in a 2 T solenoidal magnetic field. The solenoid is surrounded by the central preshower (CPS) detector located immediately before the inner layer of the electromagnetic calorimeter. The CPS consists of approximately one radiation length of lead absorber surrounded by three layers of scintillating strips. The calorimeter is composed of three sections: a central section covering the range of pseudorapidities $|\eta_{\text{det}}| < 1.1$ [22] and two end calorimeters (EC) with coverage extending to $|\eta_{\text{det}}| \approx 4.2$, with all three housed in separate cryostats. The electromagnetic (EM) calorimeter is composed of four layers of $\Delta\eta_{\text{det}} \times \Delta\phi_{\text{det}} = 0.1 \times 0.1$ cells, with the exception of layer three (EM3) with 0.05×0.05 granularity. The calorimeter resolution for measurements of the electron/photon energy at 50 GeV is about 3.6%. The energy response of the calorimeter to photons is calibrated using electrons from Z boson decays. Since electrons and photons shower differently in matter, additional corrections as a function of η are derived using a detailed GEANT-based [36] simulation of the D0 detector response. These corrections are the largest, 2.0–2.5%, at low photon energies (≈ 20 GeV). Events satisfying the following trigger requirements are recorded: at least two clusters of energy in the EM calorimeter with a loose shower shape requirement and a range of p_T thresholds between 15 GeV and 25 GeV. Luminosity is measured using plastic scintillator arrays placed in front of the EC cryostats.

Events are selected with at least two photon candidates with transverse momentum $p_T > 18$ (17) GeV for the leading (next-to-leading) candidate and pseudorapidity $|\eta| < 0.9$. We require a slight difference between the p_T cutoffs for the two photons to avoid a divergent kinematic region of the NLO calculations [19]. The trigger is more than 90% efficient for these selections.

At high instantaneous luminosities there is more than one $p\bar{p}$ interaction per beam crossing. The photon p_T is computed with respect to the reconstructed $p\bar{p}$ interaction vertex with the highest number of associated tracks, called the event vertex [15]. The event vertex is required to be reconstructed within 60 cm of the center of the detector along the beam axis (z), and satisfies this requirement in 98% of events.

Photon candidates are formed from calorimeter towers in a cone of radius $\mathcal{R} = \sqrt{(\Delta\eta)^2 + (\Delta\phi)^2} = 0.4$ around a seed tower [32]. A stable cone is found iteratively, and the final cluster energy is recalculated from the inner core within $\mathcal{R} = 0.2$. The photon candidates are required to: (i) have $\geq 97\%$ of the cluster energy deposited in the EM calorimeter layers; (ii) be isolated in the calorimeter according to $[E_{\text{tot}}(0.4) - E_{\text{EM}}(0.2)]/E_{\text{EM}}(0.2) < 0.07$, where $E_{\text{tot}}(\mathcal{R})$ [$E_{\text{EM}}(\mathcal{R})$] is the total [EM only] energy in a cone of radius \mathcal{R} ; (iii) have the scalar sum of p_T 's of all tracks originating from the event vertex in an annulus of $0.05 < \mathcal{R} < 0.4$ around the

EM cluster less than 1.5 GeV; and (iv) have an energy-weighted EM shower width consistent with that expected for an electromagnetic shower. To suppress electron misidentification as photons, the EM clusters are required to have no spatial match to a charged particle track or any tracker hit configuration consistent with an electron. The two photon EM clusters are required to be separated by $\Delta\mathcal{R}_{\gamma\gamma} > 0.4$.

An additional group of variables exploiting the differences between the photon-initiated and jet activity in the EM calorimeter and the tracker is combined into an artificial neural network (NN) to further reject jet background [38]. In these background events, photons are mainly produced from decays of energetic π^0 and η mesons. The NN is trained on γ and jet PYTHIA [39] MC samples. The generated MC events are processed through a GEANT-based simulation of the D0 detector. Simulated events are overlaid with data events from random $p\bar{p}$ crossings to properly model the effects of multiple $p\bar{p}$ interactions and detector noise in data. Care is taken to ensure that the luminosity distribution in the overlay events is similar to the data used in the analysis. MC events are then processed through the same reconstruction procedure as the data. MC events are reweighted to take into account the trigger efficiency in data, and small observed differences in instantaneous luminosity and distribution of the z coordinate of the event vertex. Photon radiation from charged leptons in Z boson decays ($Z \rightarrow \ell^+\ell^-\gamma$, $\ell = e, \mu$) is used to validate the NN performance [40]. The NN describes the data well and gives significant extra discrimination against jets. The photon candidates in this analysis are chosen such that their NN output requirement retains 98% of photons and rejects $\approx 40\%$ of jets beyond the rejection provided by the selection described above [15].

We estimate contributions from instrumental γ + jet and dijet backgrounds and also the contribution from Z boson/Drell–Yan production events $Z/\gamma^* \rightarrow e^+e^-$ (ZDY). In the instrumental backgrounds, one or more jets are misidentified as photons from jet-forming partons that hadronize into isolated neutral meson(s) (π^0 or η) giving rise to two or more photons in the final state. Electrons in the ZDY background can be misidentified as photons due to similarities in the shower shape. The contribution from the ZDY events is estimated from MC simulation with PYTHIA, normalized to the NNLO cross section [41]. On average, 2% of the electrons survive the selection criteria above, mainly due to the inefficiency of matching a charged track to an electron. In data this inefficiency is higher than in MC and the ZDY contribution is corrected for these differences, using the correction factors from $Z \rightarrow e^+e^-$ data and MC study.

The γ + jet and dijet instrumental backgrounds are estimated by fitting a two-dimensional (2D) distribution of the leading and next-to-leading photon NN outputs with templates extracted from DDP SHERPA signal and EM-jet PYTHIA MC samples. In the latter, constraints are placed at the generator level to increase the statistics of jet events fluctuating into EM-like objects [38]. For the γ + jet template, the photon candidate is taken from either the $\gamma\gamma$ sample or from the EM-jet sample, while for the dijet template, both candidates are taken from the EM-jet sample. Table 1 shows the numbers of events surviving the selection in data for different $\Delta\phi_{\gamma\gamma}$ regions, as well as the number of data events from each of the four sources as determined by a fit of the signal and background templates to data. Comparisons of signal and background templates show good agreement with NN distributions of photons from radiative Z decays and EM-jets. The latter are obtained by inverting the 0.07 calorimeter isolation cut or requiring a matching to a track [4,15] in data, respectively. The typical DDP purity in the selected data events is around 60%. We have also done cross checks by recalculating the cross sections with no or tighter cuts on the photon NN, by imposing a requirement of at least one preshower

Table 1

The numbers of $\gamma\gamma$ ($N_{\gamma\gamma}$), $\gamma j + j\gamma$ ($N_{\gamma j}$), jj (N_{jj}), and ZDY (N_{ZDY}) events and their total. The quoted uncertainties are statistical only and for $N_{\gamma\gamma}$, $N_{\gamma j}$, and N_{jj} are from 2D fitting.

	Full $\Delta\phi_{\gamma\gamma}$	$\Delta\phi_{\gamma\gamma} < \pi/2$	$\Delta\phi_{\gamma\gamma} \geq \pi/2$
$N_{\gamma\gamma}$	20255 ± 398	1676 ± 109	18572 ± 370
$N_{\gamma j}$	2575 ± 516	317 ± 148	2217 ± 459
N_{jj}	10992 ± 344	854 ± 96	10185 ± 314
N_{ZDY}	198 ± 14	2.7 ± 1.7	195 ± 13
Total	34020	2851	31169

Table 2

Total measured cross sections compared to the values calculated using SHERPA, 2 γ NNLO, DIPHOX, and RESBOS event generators. The statistical uncertainties on the theoretical predictions are negligible.

Region	σ (pb)	δ_{tot} (%)	SHERPA (pb)	2 γ NNLO (pb)	DIPHOX (pb)	RESBOS (pb)
Total	9.42	+4/−4	7.93	7.60	5.95	6.63
$\Delta\phi_{\gamma\gamma} < \pi/2$	1.48	+10/−9	1.01	0.45	0.41	0.05
$\Delta\phi_{\gamma\gamma} > \pi/2$	7.94	+5/−5	6.92	7.15	5.54	6.58

cluster inside the photon cone, or by using a matrix method as in the previous analysis [15]. All the results are consistent within uncertainties.

The estimated numbers of DDP events in each bin are corrected for the geometric and kinematic acceptance of the photon, as well as for the photon detection efficiency. Both acceptance and efficiency are calculated using SHERPA MC events. The acceptance is calculated for the events satisfying at the particle level $p_T^\gamma > 18$ (17) GeV for the leading (next-to-leading) photon, $|\eta^\gamma| < 0.9$, and $\Delta\mathcal{R}_{\gamma\gamma} > 0.4$ [42]. The photon is also required to be isolated by $p_T^{\text{iso}} = p_T^{\text{tot}}(0.4) - p_T^\gamma < 2.5$ GeV, where $p_T^{\text{tot}}(0.4)$ is the scalar sum of the transverse momenta of the stable particles within a cone of radius $\mathcal{R} = 0.4$ centered on the photon.

The acceptance is driven by selection requirements in η_{det} (applied to avoid edge effects in the calorimeter regions used for the measurement) and ϕ_{det} (to avoid periodic calorimeter module boundaries) [32], photon rapidity η^γ and p_T^γ , and bin-to-bin migration effects due to the finite energy and angular resolution of the EM calorimeter. Typically, greater than 80% of events at the reconstruction level remain in the same bin as at the particle level. We estimate the effect of selecting an incorrect vertex (in about 35% of events) using $Z \rightarrow e^+e^-$ data events, where we remove tracks corresponding to the electron and positron to model the distribution of the distance between the “true” vertex and event vertex. The choice of an incorrect event vertex leads to a systematic uncertainty on the acceptance, typically $\lesssim 3\%$ for $\Delta\phi_{\gamma\gamma} \geq \pi/2$ and $\lesssim 6\%$ for $\Delta\phi_{\gamma\gamma} < \pi/2$. The systematic uncertainty is estimated by using DDP events simulated with SHERPA in which the event vertex position is randomized according to its distribution in z with respect to the “true” vertex, obtained from the $Z \rightarrow e^+e^-$ data study, and by recalculating all relevant variables of the diphoton system. These results have also been cross-checked by using photons with preshower clusters (about 50–65% of our dataset), where the “true” vertex z position is found as a weighted average of the z positions pointed to by the two photons. Using such a pointing we are able to find the “true” vertex with a resolution of about 2.5–4.3 cm [33]. The systematic uncertainty on the acceptance due to the choice of the new vertex and recalculated photon p_T^γ and η^γ with this method is close, within 3–6% to values found from the first method using $Z \rightarrow e^+e^-$ events. The systematic uncertainty decreases towards higher diphoton $p_T^{\gamma\gamma}$ and smaller $\Delta\phi_{\gamma\gamma}$.

Possible model-dependent effects are corrected by recalculating the acceptance according to the difference between the photon p_T spectra in data and SHERPA MC. The acceptance grows from 45%

Table 3

The measured differential cross sections in bins of $M_{\gamma\gamma}$ and $p_T^{\gamma\gamma}$. The columns δ_{stat} , δ_{syst} , and δ_{tot} represent the statistical, systematic, and total uncertainties, respectively.

$M_{\gamma\gamma}$ (GeV)	$\langle M_{\gamma\gamma} \rangle$ (GeV)	$d\sigma/dM_{\gamma\gamma}$ (pb/GeV)	δ_{stat} (%)	δ_{syst} (%)	δ_{tot} (%)
30–40	37.0	1.47×10^{-1}	8	+15/–11	+17/–14
40–50	44.8	3.06×10^{-1}	4	+14/–10	+15/–11
50–60	54.5	1.44×10^{-1}	4	+11/–9	+12/–10
60–70	64.5	7.93×10^{-2}	5	+11/–9	+12/–11
70–80	74.6	4.21×10^{-2}	7	+14/–12	+16/–14
80–90	84.6	2.57×10^{-2}	7	+13/–11	+14/–12
90–100	94.8	1.53×10^{-2}	9	+14/–13	+16/–15
100–125	110.9	7.97×10^{-3}	6	+12/–10	+14/–12
125–150	136.2	2.88×10^{-3}	7	+15/–14	+16/–16
150–200	170.4	1.27×10^{-3}	7	+15/–13	+16/–15
200–350	249.2	2.66×10^{-4}	8	+15/–14	+17/–17
350–500	403.0	2.70×10^{-5}	22	+47/–47	+53/–52

$p_T^{\gamma\gamma}$ (GeV)	$\langle p_T^{\gamma\gamma} \rangle$ (GeV)	$d\sigma/dp_T^{\gamma\gamma}$ (pb/GeV)	δ_{stat} (%)	δ_{syst} (%)	δ_{tot} (%)
0.0–2.5	1.4	6.27×10^{-1}	4	+9/–9	+10/–10
2.5–5.0	3.6	5.38×10^{-1}	12	+9/–9	+15/–15
5.0–7.5	6.2	3.50×10^{-1}	14	+10/–9	+17/–17
7.5–10	8.8	3.47×10^{-1}	15	+15/–10	+22/–19
10–12.5	11.2	2.35×10^{-1}	12	+12/–11	+17/–17
12.5–15	13.7	1.77×10^{-1}	16	+12/–11	+20/–20
15–20	17.3	1.26×10^{-1}	10	+12/–11	+16/–15
20–25	22.4	6.99×10^{-2}	8	+12/–11	+15/–14
25–30	27.4	5.29×10^{-2}	10	+12/–10	+16/–15
30–40	34.8	6.32×10^{-2}	8	+12/–11	+14/–14
40–50	44.5	5.04×10^{-2}	9	+13/–13	+16/–16
50–60	54.7	2.53×10^{-2}	13	+13/–12	+19/–19
60–80	67.9	1.04×10^{-2}	12	+12/–11	+17/–17
80–100	87.7	3.45×10^{-3}	17	+20/–20	+26/–26
100–120	108.4	1.19×10^{-3}	19	+20/–19	+28/–28
120–170	139.6	4.75×10^{-4}	20	+20/–20	+29/–28

Table 4

The measured differential cross sections in bins of $\Delta\phi_{\gamma\gamma}$ and $|\cos\theta^*|$. The columns δ_{stat} , δ_{syst} and δ_{tot} represent the statistical, systematic, and total uncertainties, respectively.

$\Delta\phi_{\gamma\gamma}$ (rad)	$\langle \Delta\phi_{\gamma\gamma} \rangle$ (rad)	$d\sigma/d\Delta\phi_{\gamma\gamma}$ (pb/rad)	δ_{stat} (%)	δ_{syst} (%)	δ_{tot} (%)
0.00–0.31	0.17	2.28	22	+12/–12	+25/–25
0.31–0.63	0.46	1.93	16	+14/–13	+21/–21
0.63–0.94	0.79	5.66×10^{-1}	12	+21/–21	+25/–24
0.94–1.26	1.11	4.09×10^{-1}	13	+21/–19	+25/–23
1.26–1.57	1.42	5.62×10^{-1}	20	+18/–17	+27/–26
1.57–1.88	1.73	6.82×10^{-1}	11	+16/–14	+20/–18
1.88–2.20	2.05	1.04	8	+14/–13	+17/–15
2.20–2.51	2.37	1.65	11	+14/–12	+18/–17
2.51–2.67	2.60	3.57	13	+21/–11	+25/–17
2.67–2.83	2.75	4.98	7	+13/–11	+14/–13
2.83–2.98	2.91	1.08×10^1	6	+13/–9	+15/–11
2.98–3.14	3.08	2.75×10^1	3	+9/–8	+9/–9

$ \cos\theta^* $	$\langle \cos\theta^* \rangle$	$d\sigma/d \cos\theta^* $ (pb)	δ_{stat} (%)	δ_{syst} (%)	δ_{tot} (%)
0.0–0.1	0.05	2.58×10^1	6	+9/–8	+11/–10
0.1–0.2	0.15	2.22×10^1	4	+9/–9	+10/–10
0.2–0.3	0.25	1.91×10^1	5	+10/–9	+11/–10
0.3–0.4	0.35	1.49×10^1	5	+9/–9	+11/–10
0.4–0.5	0.45	9.91	7	+10/–9	+12/–12
0.5–0.6	0.54	5.20	9	+11/–10	+14/–14
0.6–0.7	0.64	1.73	12	+17/–17	+21/–21

in the low $M_{\gamma\gamma}$ region to 80% in the high mass region. The systematic uncertainty on the acceptance varies within 4–21%. Vertex choice, model dependence, and photon energy scale uncertainty provide the largest contributions. In the regions dominated by fragmentation photons, such as low $\Delta\phi_{\gamma\gamma}$ and intermediate $p_T^{\gamma\gamma}$, the acceptance is lower than in the regions dominated by direct production.

Table 5

The measured differential cross sections in bins of $M_{\gamma\gamma}$, $p_T^{\gamma\gamma}$, and $|\cos\theta^*|$ for $\Delta\phi_{\gamma\gamma} < \pi/2$. The columns δ_{stat} , δ_{syst} and δ_{tot} represent the statistical, systematic, and total uncertainties, respectively.

$M_{\gamma\gamma}$ (GeV)	$\langle M_{\gamma\gamma} \rangle$ (GeV)	$d\sigma/dM_{\gamma\gamma}$ (pb/GeV)	δ_{stat} (%)	δ_{syst} (%)	δ_{tot} (%)
30–40	34.3	1.64×10^{-2}	14	+14/–14	+20/–20
40–50	44.8	8.92×10^{-3}	28	+15/–14	+31/–31
50–60	54.6	2.25×10^{-3}	23	+23/–23	+33/–33
60–70	64.6	1.22×10^{-3}	41	+25/–27	+48/–49
70–90	78.7	5.60×10^{-4}	30	+14/–14	+33/–33
90–200	111.4	5.44×10^{-5}	41	+30/–30	+51/–51

$p_T^{\gamma\gamma}$ (GeV)	$\langle p_T^{\gamma\gamma} \rangle$ (GeV)	$d\sigma/dp_T^{\gamma\gamma}$ (pb/GeV)	δ_{stat} (%)	δ_{syst} (%)	δ_{tot} (%)
25–30	28.3	5.89×10^{-3}	44	+30/–28	+54/–53
30–40	35.8	3.56×10^{-2}	23	+14/–14	+27/–27
40–50	44.5	4.39×10^{-2}	15	+17/–17	+22/–22
50–60	54.8	1.72×10^{-2}	18	+14/–14	+23/–23
60–80	67.8	7.74×10^{-3}	17	+12/–12	+21/–21
80–100	87.5	2.70×10^{-3}	22	+17/–17	+28/–28
100–120	108.3	7.07×10^{-4}	17	+22/–22	+28/–28
120–170	140.5	3.84×10^{-4}	25	+26/–26	+36/–36

$ \cos\theta^* $	$\langle \cos\theta^* \rangle$	$d\sigma/d \cos\theta^* $ (pb)	δ_{stat} (%)	δ_{syst} (%)	δ_{tot} (%)
0.0–0.1	0.05	2.64	23	+23/–23	+33/–33
0.1–0.2	0.15	3.22	13	+18/–18	+23/–23
0.2–0.3	0.25	3.71	15	+14/–14	+21/–21
0.3–0.4	0.34	2.17	17	+12/–12	+21/–21
0.4–0.5	0.45	1.09	17	+15/–15	+23/–23
0.5–0.6	0.54	6.12×10^{-1}	39	+23/–23	+45/–45
0.6–0.7	0.63	3.33×10^{-1}	39	+27/–27	+48/–48

Table 6

The measured differential cross sections in bins of $M_{\gamma\gamma}$, $p_T^{\gamma\gamma}$, and $|\cos\theta^*|$ for $\Delta\phi_{\gamma\gamma} \geq \pi/2$. The columns δ_{stat} , δ_{syst} and δ_{tot} represent the statistical, systematic and total uncertainties, respectively.

$M_{\gamma\gamma}$ (GeV)	$\langle M_{\gamma\gamma} \rangle$ (GeV)	$d\sigma/dM_{\gamma\gamma}$ (pb/GeV)	δ_{stat} (%)	δ_{syst} (%)	δ_{tot} (%)
30–40	37.5	1.31×10^{-1}	9	+11/–9	+14/–13
40–50	44.8	2.96×10^{-1}	5	+9/–8	+10/–9
50–60	54.5	1.43×10^{-1}	4	+8/–8	+10/–10
60–70	64.5	8.06×10^{-2}	5	+9/–9	+10/–10
70–80	74.6	4.10×10^{-2}	8	+9/–9	+12/–12
80–90	84.6	2.53×10^{-2}	7	+12/–12	+13/–13
90–100	94.7	1.53×10^{-2}	9	+12/–12	+14/–14
100–125	110.9	7.97×10^{-3}	7	+10/–10	+12/–13
125–150	136.2	2.82×10^{-3}	8	+15/–15	+17/–17
150–200	170.4	1.26×10^{-3}	7	+13/–13	+15/–15
200–350	249.2	2.65×10^{-4}	9	+15/–15	+17/–17
350–500	403.0	2.70×10^{-5}	28	+47/–47	+55/–55

$p_T^{\gamma\gamma}$ (GeV)	$\langle p_T^{\gamma\gamma} \rangle$ (GeV)	$d\sigma/dp_T^{\gamma\gamma}$ (pb/GeV)	δ_{stat} (%)	δ_{syst} (%)	δ_{tot} (%)
0.0–2.5	1.4	6.34×10^{-1}	5	+9/–9	+10/–10
2.5–5.0	3.6	5.42×10^{-1}	16	+8/–8	+18/–18
5.0–7.5	6.2	3.52×10^{-1}	20	+9/–9	+22/–22
7.5–10	8.8	3.48×10^{-1}	14	+12/–9	+19/–17
10–12.5	11.2	2.35×10^{-1}	17	+11/–11	+20/–20
12.5–15	13.7	1.77×10^{-1}	16	+11/–11	+20/–20
15–20	17.3	1.26×10^{-1}	11	+10/–10	+15/–15
20–25	22.4	6.96×10^{-2}	9	+10/–10	+14/–14
25–30	27.3	4.82×10^{-2}	11	+12/–12	+16/–17
30–40	34.2	3.03×10^{-2}	8	+10/–10	+13/–13
40–50	44.4	1.21×10^{-2}	10	+9/–9	+14/–14
50–60	54.5	5.93×10^{-3}	14	+20/–20	+24/–24
60–80	68.2	2.18×10^{-3}	14	+16/–16	+21/–21
80–100	88.3	5.83×10^{-4}	25	+29/–29	+38/–38
100–120	108.5	4.91×10^{-4}	27	+24/–24	+36/–36
120–170	137.4	1.13×10^{-4}	30	+31/–31	+43/–43

$ \cos\theta^* $	$\langle \cos\theta^* \rangle$	$d\sigma/d \cos\theta^* $ (pb)	δ_{stat} (%)	δ_{syst} (%)	δ_{tot} (%)
0.0–0.1	0.05	2.24×10^1	6	+8/–8	+10/–10
0.1–0.2	0.15	1.86×10^1	5	+8/–8	+9/–9
0.2–0.3	0.25	1.55×10^1	6	+9/–8	+11/–11
0.3–0.4	0.35	1.24×10^1	6	+8/–8	+10/–10
0.4–0.5	0.45	8.38	8	+9/–9	+12/–12
0.5–0.6	0.54	4.43	10	+11/–10	+15/–14
0.6–0.7	0.64	1.04	17	+22/–22	+28/–28

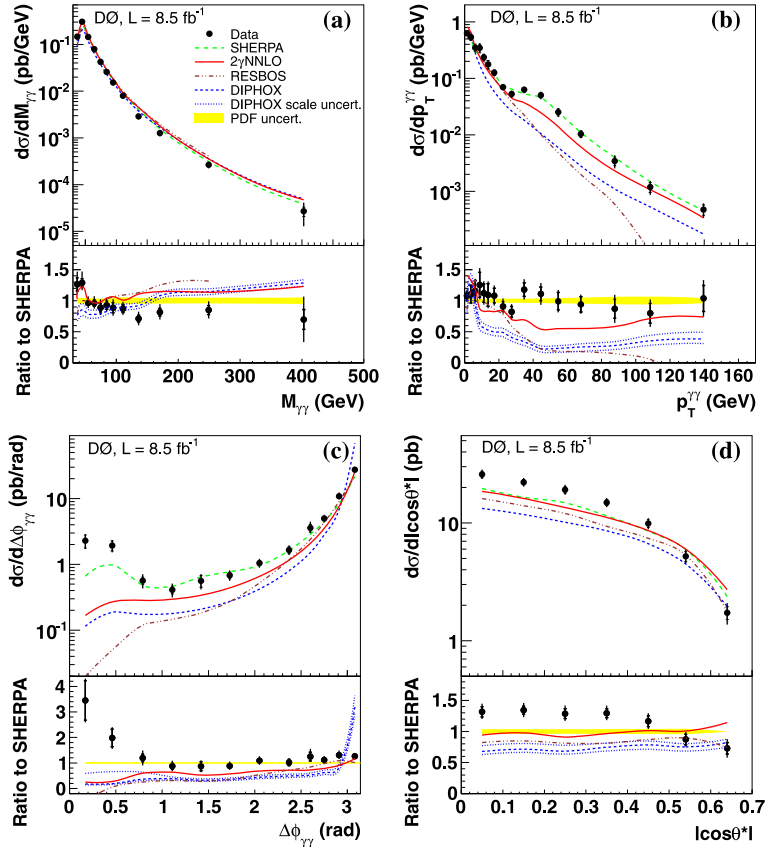


Fig. 1. (Color online.) The differential cross section as a function of (a) $M_{\gamma\gamma}$, (b) $p_T^{\gamma\gamma}$, (c) $\Delta\phi_{\gamma\gamma}$, and (d) $|\cos\theta^*|$ for the full $\Delta\phi_{\gamma\gamma}$ region from data (black points) and theory predictions (curves) are shown in the upper plots. The lower plots show the ratio of data and DIPHOX, RESBOS, and 2γ NNLO predictions to the SHERPA predictions. The inner line for the error bars in data points shows the statistical uncertainty, while the outer line shows the total (statistical and systematic added in quadrature) uncertainty after subtracting the 7.4% normalization uncertainty.

The EM clusters reconstructed in the acceptance region are required to pass the photon identification criteria listed above. Small differences between the photon identification efficiencies in data and MC are corrected by using control samples of electrons from Z boson decays and photons from radiative Z boson decays [15,40]. The overall diphoton selection efficiency is typically about 50% with variations of $\pm 5\%$. The relative systematic uncertainty of the diphoton selection efficiency is about 4%. The main contributors to the selection efficiency uncertainty are uncertainties on the electron identification efficiency, track rejection correction factors between data and MC, and efficiency differences between the photon and electron as measured in radiative Z boson decays in data and MC.

The differential cross sections $d\sigma/dM_{\gamma\gamma}$, $d\sigma/dp_T^{\gamma\gamma}$, $d\sigma/d\Delta\phi_{\gamma\gamma}$, and $d\sigma/d|\cos\theta^*|$ are calculated from the number of data events after the subtraction of background contributions divided by the event selection efficiencies, acceptance, integrated luminosity, and the bin width. We also measured the total cross sections averaged over $p_T^{\gamma\gamma}$, $\Delta\phi_{\gamma\gamma}$, and $|\cos\theta^*|$ variables, shown in Table 2. Uncertainties on the theoretical predictions are described in the text below.

The measured differential cross sections for all considered kinematic regions are presented in Tables 3–6. The average value of each variable in a bin was estimated using SHERPA MC events. The statistical uncertainty δ_{stat} is caused by finite MC statistics used for the efficiency and acceptance calculations and by the statistical uncertainty in data, taking into account statistical correlations with adjacent bins. The latter are estimated using an inverted smearing matrix, following a procedure described in Ref. [43]. The smear-

ing matrix represents the detector resolution function and relates each bin at the particle level to the bins at the reconstruction level. It is constructed for each variable using the DDP MC events simulated with SHERPA. The systematic uncertainties quoted in the tables include acceptance, trigger efficiency, photon selection efficiency, background subtraction, and 6.1% luminosity uncertainties.

Figs. 1–3 show a comparison of the measured differential cross sections to the theoretical predictions from DIPHOX, RESBOS, 2γ NNLO, and SHERPA. The RESBOS predictions are valid only for the phase space limited by $9 < M_{\gamma\gamma} < 350$ GeV. We take this into account in our calculations and compare RESBOS predictions to $M_{\gamma\gamma}$ measurements up to ≈ 250 GeV (see Table 3), the last mass value below 350 GeV where the cross section is measured. Systematic uncertainties across the bins in the measured cross sections are largely ($> 90\%$) correlated. A common normalization uncertainty of 7.4% resulting from luminosity and diphoton selection efficiency is not shown in the plots. The predictions from SHERPA, DIPHOX and RESBOS are computed using the CTQ6.6M NLO PDFs [44], and from 2γ NNLO using MSTW2008 NNLO PDFs [45]. The PDF uncertainty is estimated using DIPHOX and the 44 eigenvectors provided with the CTQ6.6M PDF set. They are found to be within 3–7%. The renormalization μ_R , factorization μ_F , and fragmentation μ_f scales are set to $\mu_R = \mu_F = \mu_f = M_{\gamma\gamma}$. The uncertainty due to the scale choice is estimated using DIPHOX via (a) a simultaneous variation by a factor of two of all scales relative to the default values and (b) considering asymmetric scales, $\mu_R = 0.5M_{\gamma\gamma}$, $\mu_F = \mu_f = 2M_{\gamma\gamma}$ and $\mu_R = 2M_{\gamma\gamma}$, $\mu_F = \mu_f = 0.5M_{\gamma\gamma}$, and taking the largest variation with respect to the default case as a systematic uncertainty. It is found to be about 10% for $d\sigma/dM_{\gamma\gamma}$ and

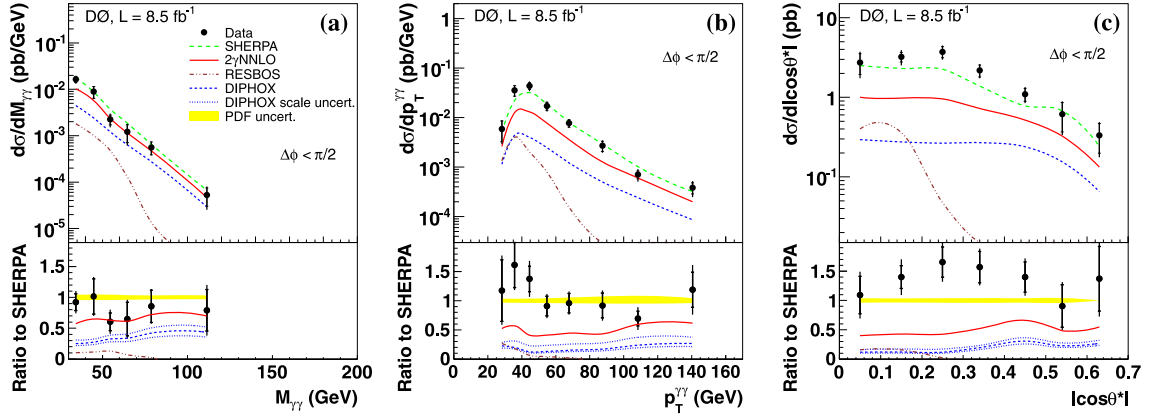


Fig. 2. (Color online.) The differential cross section as a function of (a) $M_{\gamma\gamma}$, (b) $p_T^{\gamma\gamma}$, and (c) $|\cos\theta^*|$ for the $\Delta\phi_{\gamma\gamma} < \pi/2$ region. The notations for points, lines and shaded regions are the same as in Fig. 1.

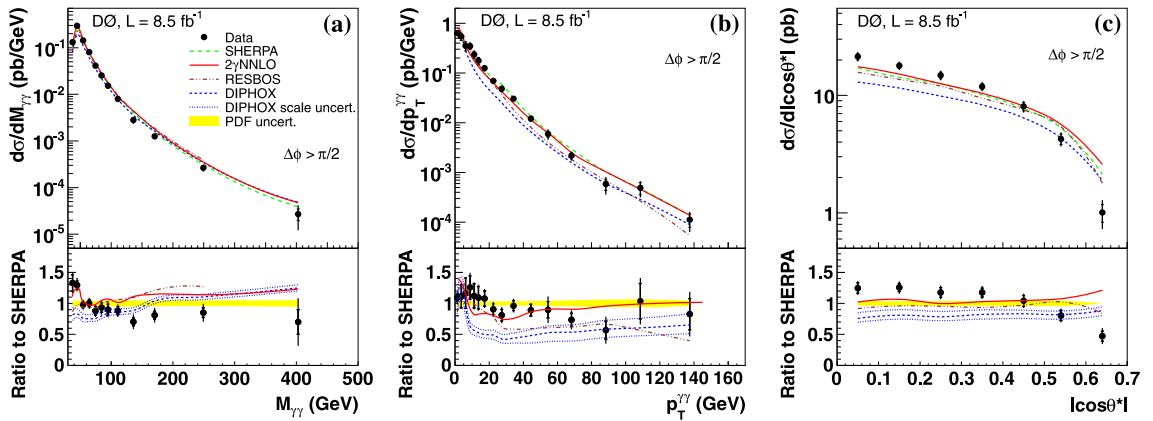


Fig. 3. (Color online.) The differential cross section as a function of (a) $M_{\gamma\gamma}$, (b) $p_T^{\gamma\gamma}$, and (c) $|\cos\theta^*|$ for the $\Delta\phi_{\gamma\gamma} \geq \pi/2$ region. The notations for points, lines and shaded regions are the same as in Fig. 1.

$d\sigma/d|\cos\theta^*|$, a maximum of 30% for $d\sigma/dp_T^{\gamma\gamma}$ at high $p_T^{\gamma\gamma}$, and up to a factor 2.5 for $d\sigma/d\Delta\phi_{\gamma\gamma}$ at low $\Delta\phi_{\gamma\gamma}$. All theoretical predictions are obtained using diphoton event selection criteria equivalent to those applied in the experimental analysis (as are those used for the acceptance calculation). In particular, the photon is required to be isolated by $p_T^{\text{iso}} < 2.5$ GeV. For DIPHOX, RESBOS, and $2\gamma\text{NNLO}$, p_T^{tot} is computed at the parton level. The cross sections from DIPHOX, RESBOS and $2\gamma\text{NNLO}$ are corrected for effects stemming from multiple parton interactions and hadronization, while for SHERPA these effects are handled within the software package. These corrections are estimated using diphoton events simulated by PYTHIA with Tunes A and S0 [39]. The corrections vary within 4–6% as a function of the measured kinematic variables and are consistent for both tunes within 1%.

Tables 3–6 show that the cross sections in the $\Delta\phi_{\gamma\gamma} \geq \pi/2$ region constitute, on average, about 85–90% of the cross sections for the full $\Delta\phi_{\gamma\gamma}$ range. From the sub-tables for the $p_T^{\gamma\gamma}$ variable, we observe that at $p_T^{\gamma\gamma} \lesssim 25$ GeV, the cross sections are fully dominated by the $\Delta\phi_{\gamma\gamma} \geq \pi/2$ region, while starting from $p_T^{\gamma\gamma} \gtrsim 30$ GeV, they are significantly dominated (by a factor of 2–4) by the $\Delta\phi_{\gamma\gamma} < \pi/2$ region. The shoulder-like structure observed in the $p_T^{\gamma\gamma}$ distribution around 30–40 GeV should be mainly caused by the fragmentation photons coming from the $\Delta\phi_{\gamma\gamma} < \pi/2$ region, and partially by higher-order (NLO and beyond) corrections [20].

In general, none of the theoretical models considered here provides a consistent description of the experimental results in all

kinematic regions. The SHERPA predictions are able to describe most of the phase space relatively well except for the low DDP mass region, very low $\Delta\phi_{\gamma\gamma}$, and with some tension in the $|\cos\theta^*|$ spectrum. A noticeable discrepancy between RESBOS and DIPHOX in some regions of the phase space is due to the absence of all-order soft-gluon resummation ($p_T^{\gamma\gamma}$ close to zero and $\Delta\phi_{\gamma\gamma}$ close to π) and the fact that the $gg \rightarrow \gamma\gamma$ contribution is calculated only at LO in DIPHOX (small $M_{\gamma\gamma}$). However, RESBOS fails to describe $M_{\gamma\gamma}$, $p_T^{\gamma\gamma}$, and $|\cos\theta^*|$ spectra in the $\Delta\phi_{\gamma\gamma} < \pi/2$ region, where the contributions from the fragmentation diagrams and higher-order corrections are important. The processes with a parton-to-diphoton fragmentation taking place at low masses ($M_{\gamma\gamma} < p_T^{\gamma\gamma}$) are not included yet in any existing calculation [10]. The regions of phase space with a significant contribution from fragmentation photons (very low $\Delta\phi_{\gamma\gamma}$) require extensive tuning of all of the considered event generators.

In summary, we have presented measurements of differential cross sections of photon pair production in $p\bar{p}$ collisions at $\sqrt{s} = 1.96$ TeV as functions of $M_{\gamma\gamma}$, $p_T^{\gamma\gamma}$, $\Delta\phi_{\gamma\gamma}$, and $|\cos\theta^*|$ for photons with $p_T > 18$ (17) GeV and $|\eta| < 0.9$ in the full $\Delta\phi_{\gamma\gamma}$ range and for $\Delta\phi_{\gamma\gamma} < \pi/2$, $\Delta\phi_{\gamma\gamma} \geq \pi/2$ separately. The cross sections are compared to the predictions made by the DIPHOX, RESBOS, $2\gamma\text{NNLO}$ and SHERPA MC generators. Overall, SHERPA provides the best description of the measured cross sections. The experimental results show discrepancies with all theoretical predictions in the regions of small $\Delta\phi_{\gamma\gamma}$ (< 0.7) and small diphoton mass (< 50 GeV) for $\Delta\phi_{\gamma\gamma} \geq \pi/2$, with some differences in the shapes

of the $|\cos\theta^*|$ distribution that may be an issue for the reliable extraction of the Higgs boson spin using the $\gamma\gamma$ final state. The results are important for understanding of DDP production and tuning of modern generators to study SM phenomena and search for beyond the SM processes.

Acknowledgements

We thank the staffs at Fermilab and collaborating institutions, and acknowledge support from the DOE and NSF (USA); CEA and CNRS/IN2P3 (France); MON, NRC KI and RFBR (Russia); CNPq, FAPERJ, FAPESP and FUNDUNESP (Brazil); DAE and DST (India); Colciencias (Colombia); CONACyT (Mexico); NRF (Korea); FOM (The Netherlands); STFC and the Royal Society (United Kingdom); MSMT and GACR (Czech Republic); BMBF and DFG (Germany); SFI (Ireland); The Swedish Research Council (Sweden); and CAS and CNSF (China).

References

- [1] G. Aad, et al., ATLAS Collaboration, Phys. Lett. B 716 (2012) 1.
- [2] S. Chatrchyan, et al., CMS Collaboration, Phys. Lett. B 716 (2012) 30.
- [3] V.M. Abazov, et al., D0 Collaboration, Phys. Rev. Lett. 107 (2011) 151801.
- [4] V.M. Abazov, et al., D0 Collaboration, Phys. Rev. D (2013), in press, arXiv:1301.5358.
- [5] T. Aaltonen, et al., CDF Collaboration, Phys. Lett. B 717 (2012) 173.
- [6] V.M. Abazov, et al., D0 Collaboration, Phys. Rev. Lett. 102 (2009) 051601.
- [7] T. Aaltonen, et al., CDF Collaboration, Phys. Rev. D 83 (2011) 011102(R).
- [8] S. Mrenna, J. Wells, Phys. Rev. D 63 (2001) 015006, and references therein.
- [9] V.M. Abazov, et al., D0 Collaboration, Phys. Lett. B 659 (2008) 856.
- [10] C. Balazs, E.L. Berger, P. Nadolsky, C.-P. Yuan, Phys. Rev. D 76 (2007) 013009.
- [11] E. Bonvin, et al., WA70 Collaboration, Z. Phys. C 41 (1989) 591;
- [12] M. Begel, PhD thesis, University of Rochester, 1999, FERMILAB-THESIS-1999-05.
- [13] C. Albajar, et al., UA1 Collaboration, Phys. Lett. B 209 (1988) 385.
- [14] J. Alitti, et al., UA2 Collaboration, Phys. Lett. B 288 (1992) 386.
- [15] V.M. Abazov, et al., D0 Collaboration, Phys. Lett. B 690 (2010) 108.
- [16] T. Aaltonen, et al., CDF Collaboration, Phys. Rev. Lett. 107 (2011) 102003.
- [17] G. Aad, et al., ATLAS Collaboration, Phys. Rev. D 85 (2012) 012003.
- [18] S. Chatrchyan, et al., CMS Collaboration, J. High Energy Phys. 1201 (2012) 133.
- [19] T. Binoth, J.Ph. Guillet, E. Pilon, M. Werlen, Eur. Phys. J. C 16 (2000) 311.
- [20] T. Binoth, J.Ph. Guillet, E. Pilon, M. Werlen, Phys. Rev. D 63 (2001) 114016.
- [21] J.C. Collins, D.E. Soper, Phys. Rev. D 16 (1977) 2219.
- [22] The polar angle θ is defined with respect to the positive z axis, which is along the proton beam direction, while the azimuthal angle ϕ is defined with respect to the x axis. Pseudorapidity is defined as $\eta = -\ln[\tan(\theta/2)]$. Also, $|\eta_{\text{det}}|$ and $|\phi_{\text{det}}|$ are the pseudorapidity and the azimuthal angle defined with respect, to the geometric center of the D0 detector.
- [23] P. Nadolsky, C. Balazs, E. Berger, C.-P. Yuan, Phys. Rev. D 76 (2007) 013008.
- [24] C. Balazs, E. Berger, S. Mrenna, C.-P. Yuan, Phys. Rev. D 57 (1998) 6934.
- [25] S. Catani, L. Cieri, D. Florian, G. Ferrera, M. Grazzini, Phys. Rev. Lett. 108 (2012) 072001.
- [26] T. Gleisberg, et al., J. High Energy Phys. 0902 (2009) 007. We use SHERPA v. 1.2.2.
- [27] S. Höche, S. Schumann, F. Siegert, Phys. Rev. D 81 (2010) 034026. As suggested by the SHERPA authors, we choose $Q_{\text{cut}} = 10$ GeV as the ME-PS matching scale and parameter $D = 0.4$ taken to be of the size of the photon isolation cone.
- [28] S. Catani, B.R. Webber, G. Marchesini, Nucl. Phys. B 349 (1991) 635.
- [29] A. Banfi, G.P. Salam, G. Zanderighi, J. High Energy Phys. 0505 (2005) 073.
- [30] S. Schumann, F. Siegert, private communication.
- [31] S. Catani, M. Grazzini, Phys. Rev. Lett. 98 (2007) 222002.
- [32] V.M. Abazov, et al., D0 Collaboration, Nucl. Instrum. Methods Phys. Res. Sect. A 565 (2006) 463.
- [33] V.M. Abazov, et al., D0 Collaboration, arXiv:1301.5358.
- [34] M. Abolins, et al., Nucl. Instrum. Methods Phys. Res. Sect. A 584 (2008) 75.
- [35] R. Angstadt, et al., Nucl. Instrum. Methods Phys. Res. Sect. A 622 (2010) 298.
- [36] R. Brun, F. Carminati, CERN Program Library Long Writeup W5013, 1993, unpublished.
- [37] T. Andeen, et al., FERMILAB-TM-2365, 2007.
- [38] V.M. Abazov, et al., D0 Collaboration, Phys. Rev. Lett. 102 (2009) 231801.
- [39] T. Sjöstrand, S. Mrenna, P.Z. Skands, JHEP 0605 (2006) 026. We use PYTHIA version v6.420 with tune A.
- [40] V.M. Abazov, et al., D0 Collaboration, Phys. Lett. B 653 (2007) 378.
- [41] R. Hamberg, W.L. van Neerven, T. Matsuura, Nucl. Phys. B 359 (1991) 343;
- [42] R. Hamberg, W.L. van Neerven, T. Matsuura, Nucl. Phys. B 644 (2002) 403 (Erratum).
- [43] C. Buttar, et al., arXiv:0803.0678 [hep-ph], Section 9.
- [44] V.M. Abazov, et al., D0 Collaboration, Phys. Rev. D 83 (2011) 052008.
- [45] J. Pumplin, et al., J. High Energy Phys. 0207 (2002) 012;
- [46] D. Stump, et al., J. High Energy Phys. 0310 (2003) 046.
- [47] A.D. Martin, W.J. Stirling, R.S. Thorne, G. Watt, Eur. Phys. J. C 63 (2009) 189.